The Potential of Refractive Index Nanobiosensing Using a Multi-Band Optically Tuned Perfect Light Metamaterial Absorber

Zohreh Vafapour, *Member, IEEE*, Hossain Ghahraloud, *Member, IEEE*, Afsaneh Keshavarz, Md. Saiful Islam, *Member, IEEE*, Ali Rashidi, Mitra Dutta, *Fellow, IEEE*, and Michael A. Stroscio, *Fellow, IEEE*

***Abstract*—An optically tunable perfect light absorber as a refractive index (RI) metamaterial (MM) nanobiosensor (NBS) is designed for sensing chemicals, monitoring the concentration of water-soluble glucose, and detecting viruses. This plasmon induced tunable metasurface works based on multi-band super-absorption in the infrared frequency regime. It consists of a metal mirror that facilitates the MM to work as an absorber where the metal pattern at the top layer creates an enhanced evanescent wave that facilitates the metasurface to work as a RI optical sensor. The modelling and numerical analysis are carried out using Finite Difference Time Domain (FDTD) method-based software, CST microwave studio where a genetic algorithm (GA) is used to optimize the geometric parameters. We demonstrate multiband super-absorption spectra having maximum absorption of more than 99%. Furthermore, we show how the multiband super-absorber nanostructure can be used as a RI NBS, where the resonance frequency shifts with the RI of the surrounding medium. The achieved opto-chemical sensitivity is approximately 65*nm*/*RIU RIU*, the bio-optical sensitivity to detect viruses is approximately 76 nm / RIU; and the optical sensitivity of the water-soluble glucose concentration is about 300*nm*/*RIU*; all sensitivities are comparable in comparison with the reported values in the literature.**

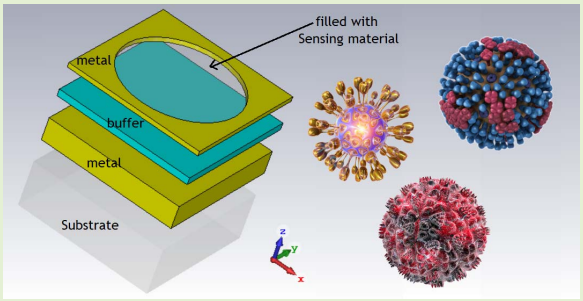

***Index Terms*—Optical nano sensor, optical virus detection, metamaterials (MMs), nano plasmonics, thin film sensors, refractive index (RI) Sensor, multi-band light absorber, perfect absorber.**

Manuscript received February 11, 2021; revised March 10, 2021; accepted March 31, 2021. Date of publication April 2, 2021; date of current version June 14, 2021. The associate editor coordinating the review of this article and approving it for publication was Dr. M. Jaleel Akhtar. *(Corresponding author: Zohreh Vafapour.)*

Zohreh Vafapour is with the Department of Bioengineering, University of Illinois at Chicago, Chicago, IL 60607 USA, and also with the Department of Electrical and Computer Engineering, University of Illinois at Chicago, Chicago, IL 60607 USA (e-mail: z.vafapour@gmail.com; zvafa@uic.edu).

Hossain Ghahraloud is with the Department of Chemical and Biomolecular Engineering, Johns Hopkins University, Baltimore, MD 21218 USA, and also with the Department of Chemical Engineering, Shiraz University, Shiraz 71345, Iran.

Afsaneh Keshavarz is with the Department of Physics, College of Science, Shiraz University, Shiraz 71946, Iran.

Md. Saiful Islam is with the School of Electrical and Electronic Engineering, University of Adelaide, SA 5005, Australia.

Ali Rashidi is with the Russell H. Morgan Department of Radiology and Radiological Science, The Johns Hopkins School of Medicine, Baltimore, MD 21287 USA.

Mitra Dutta is with the Department of Electrical and Computer Engineering, University of Illinois at Chicago, Chicago, IL 60607 USA, and also with the Department of Physics, University of Illinois at Chicago, Chicago, IL 60607 USA.

Michael A. Stroscio is with the Department of Bioengineering, University of Illinois at Chicago, Chicago, IL 60607 USA, also with the Department of Electrical and Computer Engineering, University of Illinois at Chicago, Chicago, IL 60607 USA, and also with the Department of Physics, University of Illinois at Chicago, Chicago, IL 60607 USA.

Digital Object Identifier 10.1109/JSEN.2021.3070731

I. Introduction

LIGHT absorption in plasmonic nanostructures has recently attracted significant interest in applications such as solar cells [1], [2], metamaterials (MMs) [3]–[7], photodetectors [8], [9], sensors [6]–[13], detectors [14]–[16], nanoimaging [17]–[19], slow light devices [20]–[24], and thermal emitters [25]–[27]. One of the most important types of MMs that has recently attracted considerable attention of many researchers is the MM perfect absorber (MMPA). MMPAs are periodic structures that absorb a large part of the incident light and have little transmission and reflection. The light scattered by the nanoparticles is trapped inside a dielectric matrix, demonstrating an effective absorption near unity. Today, it is well understood that anomalous light absorption in metal structures is due to the excitation of surface plasmon polaritons (SPPs). However, the MMPAs based on the excitation of SPPs has the common problem of single band, which greatly limits its application especially for infrared detection and imaging devices.

The importance in designing the MMPAs is that they consist of a metal layer with a thickness greater than the skin depth, which prevents the transmission of incident light. Additionally, the structure must include a thin metal film

with a design (H-shape, ring, square or any other resonator shape) that is separated from the previous metal layer by a dielectric spacer which is called buffer layer. If the geometry of this thin metal film is engineered in such a way that the impedance of the structure perfect matches with the impedance of free space, it will reduce the reflection of the incident light. Thus, in the structure, transmission, and reflection decrease, so, the absorption increases. In the other words, we observe the locally intense concentration of the electromagnetic (EM) wave in the structure that is due to the interaction of light and matter. MMPAs have significant applications, including sensors [27], [28], absorption filtering [29], etc. The design of the MMPAs can be such that absorption occurs at various frequency ranges including GHz [30], THz [31]–[33], IR and optical frequencies [34].

MMPAs are available in a variety of types, including single band [6], [25], multi-band [31], [32], narrow band [25], [35], broadband [18], [36], [38], etc. Each of these attributes is applied to a specific application. For example, multi-band adsorption is required in detecting and imaging applications. Since multi-band absorbers have the potential for frequency selective detection, they reduce environmental disturbance and increase the sensitivity of detection and image resolution. To achieve multi-band absorption, a direct and usual strategy is to combine several different sized periodic metallic resonators to realize the super resonators [6], [37], [38], [39]. Recently, researchers have achieved single- [40], dual- [41], [42] and multi-band MMAs [6], [37], [38], [39] and perfect absorbers [6], [43], [44], [45], [46].

One of the most important applications of MMPAs is detecting and sensing in plasmonic structures. In this case, with a very small change in the refractive index (RI) of the material surrounding the MMPAs, there are many changes in the absorption rate and frequency. The change in the RI of the surrounding material in the MMPA structures causes a change in the impedance matching conditions, and thus the absorption rate and frequency vary for different materials. Therefore, the MMPA is a great candidate to detect materials that have close RI values [6]. The sensitivity of the RI is strongly influenced by local electric fields and the interaction of hot spots with the material which intend to sense [16], [32]. Therefore, MMPAs are very suitable for detecting the RI of materials.

The achievement of narrow peak, multi-peak, and broad-band absorption which deal with different applications are still significant issues in the optics and photonics research. This article is intended to provide a general overview of the different optical RI NBS applications in progress in the proposed optical design. We have divided them into three different categories based on the materials used to sense/detect. In the next section, we will introduce the structural design, the optical and geometrical parameters of the proposed nanostructure. Section 3 will outline the main physical concepts underlying absorption such as excitation of the SPPs and its applications in optical sensors, the ability to realize tunability of the proposed multi-band PA and analyzing the EM field distributions. We will discuss our advances in processing of optical RI NBS, in the fourth section of this study. Our developments related to opto-chemical, and biomedical sensing for virus detection and glucose concentration sensing are presented in detail.

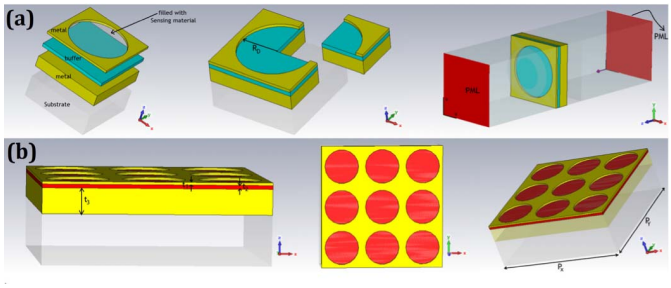

Fig. 1. The unit cell schematic of the nanostructure designed. a) The 3D schematic illustration of the simulation environment and conditions. (b) The lower panel illustrates that periodic design of the whole structure resides on a glass substrate; the left panel shows the side-view (from Y-direction) of the nanostructure, and the right panels show a top-view of the nanostructure.

II. Structure Description

Figure 1(a) shows a unit cell of the perfect light MM absorber nanostructure which referred "MMPA". As illustrated in Fig. 1(a), the nanostructure is designed to have a metal–dielectric–metal sandwich model containing periodic metal circulator particles and a metal film, separated by a magnesium fluoride (MgF_2) dielectric spacer layer as a buffer. Note that, we run genetic algorithm (GA) as an optimization tool to optimize different parameters. The goal is to achieve maximum absorption. The population size, number of iterations and mutation rate is set to 30 iterations, and a mutation rate of 70% is applied. The optimized values obtained using GA are as followed. The thickness of the circular metallic particle is denoted by $t_1 = 20\ nm$ and its radius is $R_D = 250\ nm$. The thicknesses of the MgF_2 layer and the metal film are represented by $t_2 = 30\ nm$ and $t_3 = 200\ nm$, respectively; and the lattice constant is $P_x = P_y = 600\ nm$. The metal layer is thick enough that no transmission can occur when light is incident from above the designed nanostructure. Because of EM resonance in the nanostructure, optical reflections from the surface can be eliminated when the nanostructured surface is designed to have the proper radius. The whole structure is located on a glass substrate with a dielectric constant and thickness of 2.4025 and 400 nm, respectively.

The design simulations are performed by using the finite difference time domain (FDTD) technique [47] package of the CST Microwave Studio. We first perform numerical calculations to investigate the relationship between the absorption spectrum and the geometric dimensions of the nanostructure to design a MMPA with a set of practicable parameters around optical communication wavelengths. The Drude model is based on measurement data is used for the electric permittivity of the metal [48]. The optical constant of MgF_2 is obtained from Ref. 47. The boundary conditions are set so that the unit cells are periodic in the E–H plane. So, the simulation domain has periodic boundary conditions in the lateral directions. The EM wave is polarized in such a way that the wave vector is perpendicular and goes to the front of the slab and the E- and H-fields are parallel to the X- and Y-directions, respectively (see Fig. 1). The periods of the unit cells are

identical in both lateral dimensions to ensure polarization independence at the normal incidence as shown in Fig. 1b. The environment in the simulations is defined as a free space which corresponds with the previous experimental method.

III. Absorption and Physical Concepts

The absorbance is calculated from the reflectance ($R(\omega) = |S_{11}(\omega)|^2$) and transmittance ($T(\omega) = |S_{21}(\omega)|^2$) which are expressed by the S_{11} and S_{21} parameters, respectively, as $A(\omega) = 1 - R(\omega) - T(\omega)$. There exists an optimal thickness of the dielectric layer (t_2) that maximizes the absorption. For the present geometry, when $t_2 = 30\ nm$, the reflectance approximately vanishes, and the absorbance can be as high as 99.99% at both frequency modes of 217 THz and 426 THz. High absorption is attributed to variation in the near field plasmon coupling between the metal circular particle and the continuous metal film.

A. Surface Plasmon Polaritons: Physics and Applications

Surface plasmon polaritons (SPPs) are surface EM excitation waves that propagate along the interface between a metal film/antenna and a dielectric material. It is well known that a metal surface can support SPP modes which are coupled modes of photons and plasmons. The surface EM waves consist of surface charges and they propagate along the surface as well as decay exponentially away from the surface. Control and manipulation of light using SPPs on the nano meter scale exhibit significant advantages in nano and biophotonics devices with very small elements; in addition, the light can also be coupled to the SPP using an optical waveguide coupler. The SPPs open a promising way in applications involving opto-chemical, thermo-optical, biological, biomedical and food industry, and research is needed to achieve useful applications.

B. Actively Tuned Multi-Band Perfect Absorber

Fig. 2(a) shows the calculated absorption spectra of the proposed multi-band absorber using silver as a metal layer and metal thin film. It is obvious that in the optimized case (i.e. $R_D = 250\ nm$), the absorber consists of three discrete absorption peaks between 150 to 450 THz frequency range located around at $f_1 = 216.6\ THz$, $f_2 = 366\ THz$, and $f_3 = 424.8\ THz$, each with absorption high over 99%. As clearly seen in Fig. 2(a), decreasing the radius of the cut-out disk (R_D) in the thin metal film causes decrease the absorption peak high and a red shift in the peak position, because the SPPs cannot couple strongly with the incident light. In Fig. 2(b), we use gold as a metal layer and metal thin film. By decreasing R_D from 250 nm to 50 nm by step of 50 nm, the absorption peak high is decreased and red shifted. The maximum absorption is about 71.6% at 213.5 THz in the optimum case of $R_D = 250\ nm$ using gold. So, we chose $R_D = 250\ nm$ as an optimum case and did all the following simulations in this case by changing metal layers and dielectric sensing materials.

In the following, we investigate the effect of different metals on absorption peak frequency position and high of the absorption peak in the optimum case of $R_D = 250\ nm$. As seen in

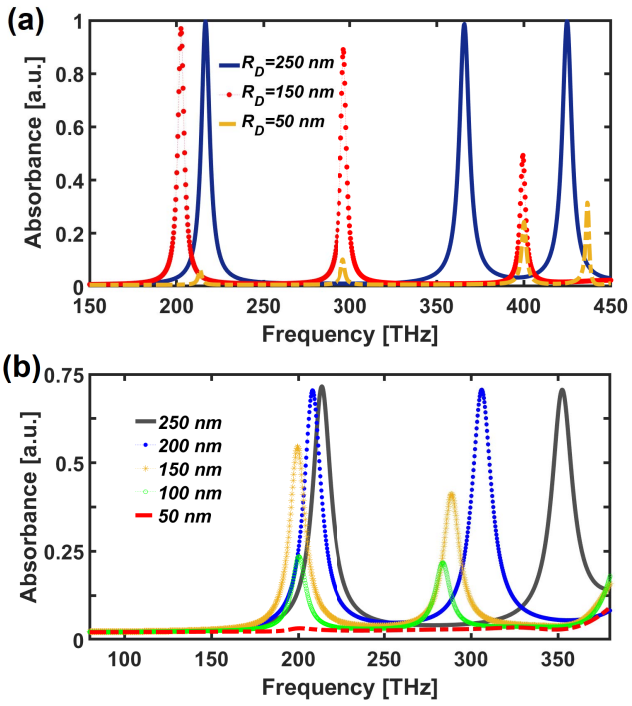

Fig. 2. The effect of changing of cut-out disk radius (R_D) on Absorbance spectra using (a) silver, and (b) gold material as a metal layer and thin film.

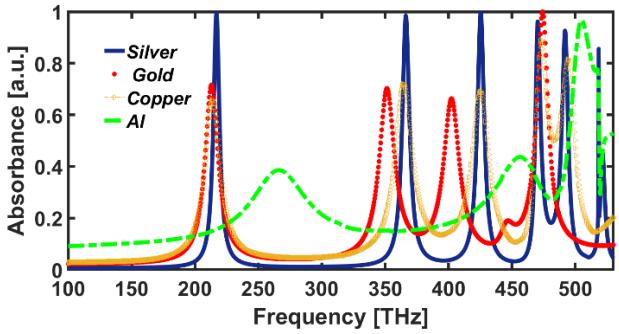

Fig. 3. The simulated results of absorbance spectrum using MgF_2 as a dielectric layer for different metals.

Fig. 3, with changing the material of the thin film and metal circulator particles from silver to copper, the absorption peak frequency positions have changed slightly (a red shift), but the absorption peak high is decreased from 99.7% (the third peak at 425.5 THz using silver) to 69.1% (the third peak at 425.1 THz using copper). When we use gold, the absorption peak frequency positions have red shifted, and the maximum absorption peak high is decreased from 99.7% for silver to 66.3% (the third peak at 402.3 THz using gold). But as obviously can be seen in Fig. 3, for aluminum (green-dotted curve), there are just three broaden absorption peaks which are not as high as in the case of silver; and the absorption peak frequency positions have a blue-shift with respect to other metals used. It should be mentioned that the broadening of the spectral response in Fig. 3 for aluminum is a result of the higher collision frequency of aluminum compared to other three metals used in this work [26]. Therefore, by analyzing

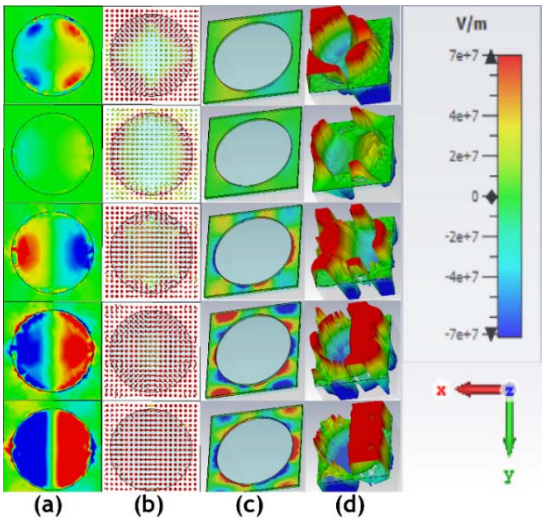

Fig. 4. The Electric field distributions (E_x) and Surface current flows of the nanostructure for five different frequency modes (f_1, f_2, f_3, f_4, and f_5) from x-y plane view for the (a) thin film layer and (b) the cut-out circular film.

the results, we decided to choose silver as a fixed material as a thin metal film and metal circulator particles and do all the following simulation in this case by only changing dielectric sensing materials.

C. Electromagnetic Field Distributions

To better understand the underlying physics, the field patterns of $|E_x|$ as electric field distributions and the surface currents corresponding to the five absorption modes (f_1, f_2, f_3, f_4, and f_5) presented in Fig. 4. The absorbance at the resonance modes is close to 99.96%, 98.46%, 99.62%, 96.19% and 92.66%, respectively; this shows the optical loss of the two last modes are bigger than those of the first three resonance modes. Different field distributions are observed for the frequencies at $f_1 = 216.6\ THz$, $f_2 = 366\ THz$, $f_3 = 424.8\ THz$, $f_4 = 484\ THz$ and $f_5 = 491.7\ THz$. As shown in Fig. 4(a), the distributions of the electric fields in the three first resonance modes are mainly focused on the metal circulator cut-out layer which is filled with the dielectric. It means that the three first resonance modes are localized EM resonance [2], [27], [32], [38]. Great enhancement of the electric field in the thin film and metal circulator cut-out layer for f_4 and f_5 absorption resonance modes indicate that the larger charge accumulates at the edges of the metal circulator cut-out layer. The obvious standing wave in X-Y plane view indicates that the guided-mode resonance occurs in the dielectric layer. As a result, light is absorbed in the dielectric layer.

It is obvious that the distribution of the electric field for the resonance modes are gathered in the inner edges of the metal circulator cut-out layer which is filled with the dielectric materials that wants to detect/sense (see Fig. 4b). They are growing to the center of the metal circulator cut-out. For the last two resonance modes (i.e., f_4 and f_5), one can see that the electric fields (see Fig. 4c) are growing up to the middle of the metal circulator cut-out layer and this shows that there is more optical loss in the last two resonance modes. The electric fields in both sides of the dielectric circular particle are canceling out each other which causes the reduction in absorption of the resonance spectrum as can be seen in Fig. 3. The electric field is mainly at the surface of structure and the area of circular dielectric of the unit cell (see Fig. 4d). As a result, based on the combination of the fundamental resonance, excitation of the SPPs and high-order resonance modes of the nanostructure, a multi-band absorber is obtained. This suggests a new way to obtain a multi-band absorber by integrating some different modes in a single nanostructure.

IV. RI Sensing Applications

Since the dielectric constant and corresponding to that, the RI of the environmental medium has an influence on the SPPs excitation, employing SPPs for optical detection will rely on the optical properties' alteration of the surrounding medium. For instance, when a metallic film or nanoparticle is exposed to light incident, there are special spectral responses such as transmission, reflection, and absorption spectra; but by adding the special material in the MM design, the spectral responses will change due to the environment close to the surface which undergoes substantial modifications based on the amount of the RI of the biomarker/biomolecule which triggers detection. The second factor which strongly influences the excitation of the SPPs is the capability of a coordinated ligand to increase or decrease the electron density in nanoparticles. Here, we investigate the RI NBS applications of the proposed perfect optical absorber. As shown in this section, we demonstrated three different optical sensing applications. The first one is chemical sensing which is a great application in chemical science and engineering and shows the proposed optical absorber can sense different chemical materials with different refractive indexes. The second sensing application is biomedical sensing which can detect the different viruses such as HSV, Influenza A, HIV and M13 bacteriophage viruses which is so important in biomedical and health science. The last one is the determination of glucose concentration, which is useful in food industry applications.

A. Opto-Chemical Sensing

Optical chemical (opto-chemical) sensors have been the focus of much research and attention in recent years because of their importance in industrial, environmental, and biomedical applications [13], [48], [50], [51]. This class of sensors combines chemical and biological recognition with advances in optoelectronics technologies. Opto-chemical sensors represent a group of chemical sensors in which electromagnetic (EM) radiation is used to generate the spectral responses in a waveguide. The interaction of the light radiation with the chemical sample is evaluated from the change of a particular optical parameter and is related to the spectral responses.

Typically, an opto-chemical sensor consists of a chemical recognition (sensing material) coupled with an optical MM design/device which consists of a waveguide, substrate, dielectric spacer, buffer material/layer and some antenna elements (Fig. 1). The function of the sensing elements/molecules are fulfilled in many cases by a cut-out circular element which can interact with the normal incident light. Once the RI is varied

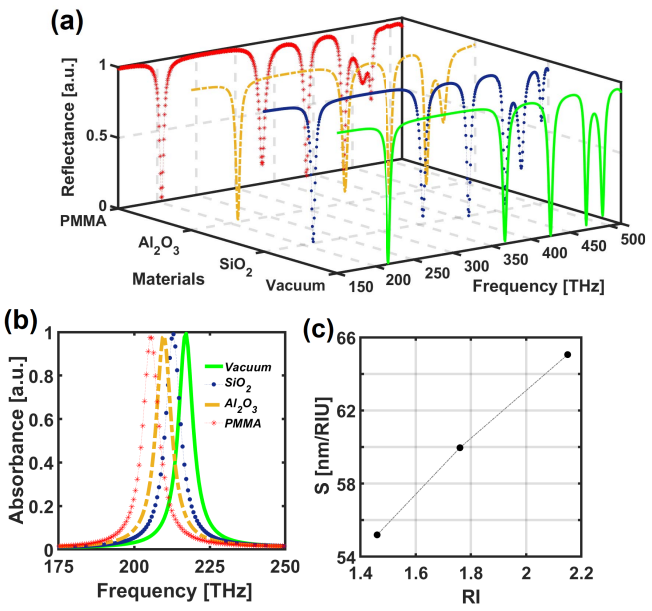

Fig. 5. (a) The 3D plot of the reflectance spectra using different dielectric spacer layer, and (b) the 2D plot of the absorbance vs frequency. And (c) The Sensitivity vs. RI.

from 1.00 ($Vacumm$) to 1.46 (SiO_2), 1.76 (Al_2O_3) and 2.15 ($PMMA$), it is obvious the frequency change for mode f_1 (the first peak of absorbance) is obvious red shift of the mode (see Fig. 5 a, b).

The full width at half maximum (FWHM) is the width of a line shape at half of its maximum amplitude which will be used in calculating sensitivity. The sensitivity is defined as the amount of frequency shift over the refractive index change (RIU) which is a comprehensive parameter to evaluate the performance of an SPR sensor. As can be seen in Fig. 5c, the maximum amount of sensitivity is $65nm/RIU$ for $PMMA$ sensing with RI of 2.15 for the investigation of the first absorption mode using silver as metal films.

B. Biomedical Sensing in Virus Detection Applications

Nano plasmonic and nano biophotonics and, in particular, biomedical applications are experiencing an increasing trend towards better, less expensive and more compact systems, either for diagnostic or treatment uses or in remote patient care. Although the trend has accelerated in the last few years, biophotonics has been always a topic close to the developments on optical biosensor and detector [5], [10], [11], [15], [28], where applications in fields of sensing and detecting the bio markers/materials based on changes in RI of the surrounding medium, in theorical, numerical and experimental aspects have been demonstrated. Here, we investigate the detection/sensing of four different viruses with different refractive indices. We explained in detail the viruses that we use to detect in this research as following.

1) HSV Virus: Herpes simplex virus (HSV) is a member of Herpesviridae virus family [52]–[54] and is categorized as a DNA virus [54]. HSV has two serotypes: HSV type 1 (HSV-1) which commonly involves the oral mucosa and the ocular region and HSV type 2 (HSV-2) which mostly is the cause of genital tract manifestations [53]–[55]. HSV-1 and HSV-2 reside in up to 90% [54] and 25% of the world's population, respectively and are the cause of morbidity and mortality in patients with immunocompromised diseases [55]. Direct contact is the main direction of the virus spreading to the host mucus membrane [56]. After the first infection by involvement of the mucosal epithelial cells and suppression by the immune system, virus causes a latent lifelong infection by involving neural cells and will be reactivated due to immunocompromised conditions [53]. HSV can be diagnosed based on the clinical presentation; however, there is limitation in the accuracy of diagnosis due to the change of the clinical picture while the disease is progressing. Thus, laboratory confirmation is essential for accurate diagnosis. Viral antigen detection, virus culture, molecular biology, and cytological examination are common laboratory methods for diagnosis of HSV infection [57].

2) Influenza A Virus: Influenza virus is an RNA virus [58] with three types — including A, B and C — that frequently causes human infection. The virus affects the upper respiratory tract as an acute viral infection that is mostly self-limited; however, it may cause severe disease and complications in up to 5 million people and up to 500,000 deaths annually [59], [60]. Although the presentation of influenza may vary based on the age groups, most common manifestations are fever, cough, sputum, rhinorrhea and myalgia among different age groups [61].

Influenza types A and B are responsible for seasonal epidemics that occurs annually [59], [62]. In addition, influenza type A by using a mechanism to change the surface protein and antigenic variation, may cause sporadic pandemics [62]. The diagnosis of influenza based on the clinical symptoms, due to the non-specificity of symptoms, is not accurate. Thus, laboratory studies with the aim of appropriate therapeutic approach identification, were initiated. Conventional, serological and molecular diagnostic methods are available methods for diagnosis of influenza [63].

3) HIV Virus: Human immunodeficiency virus (HIV) is an RNA virus and a member of Retroviridae family [64]. The viral infection by weakening of the immune system and involvement of multiple systems causes acquired immunodeficiency syndrome (AIDS) [64], [65]. Based on the United Nations report, at the end of 2018, about 37.9 million people are living with HIV infection in the world and newly infected people with HIV were estimated as about 1.7 million people [66]. Since the virus cannot survive outside of the human body, direct exchange of bodily fluid through blood-borne, sexually, or perinatal is needed for the virus transmission [65], [66]. CD4 + T cells are the main goal of the virus that by contamination of these cells, causes immunosuppression and results in disease morbidity and mortality. In individuals with HIV infection, CD4 + T cells counts are considered as an indicator of immunosuppression [65]. According to the US Preventive Services Task Force, all 13 to 64 years patients, regardless of known risk, be offered HIV testing at least once in the life [67]. Currently, enzyme-linked immunosorbent assay (ELISA), Western blot (WB), and polymerase chain reaction (PCR) are available diagnostic tests for HIV infection; however, due to need of trained personnel and infrastructures,

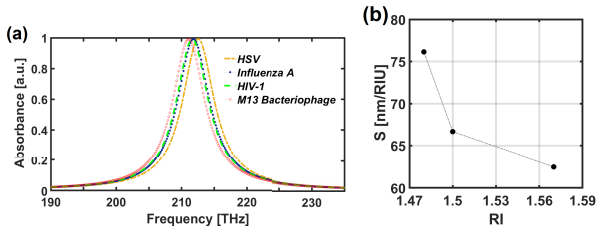

Fig. 6. The reflectance spectra of the different viruses having different RI values and (b) The reflectance spectra of the different viruses having different RI values vs. frequency.

the use of these methods is limited to central laboratories. In addition, the rapid antigen/antibody tests, that is available for diagnosis of HIV, have the limitation of diagnosis in infants and recently infected patients [68].

4) M13 Bacteriophage: Bacteriophages, also known as bacterial viruses, are one of the genetic elements in prokaryotic cells and classified as 'mobile genetic elements' [69]. These biological entities are found in different environments on the planet, such as hypersaline environments, the soil, deserts, Polar Regions, and also within other organisms [70]. The role of bacteriophages is not clearly understood yet; however, modulation of the bacterial population by the ability to kill host bacteria, gene transfer among themselves or species, and competition mediators among different species, were noted as most probable bacteriophages roles [70], [71]. During the past 70 years, the electron microscope has provided more details of bacteriophages. Accordingly, the diagnosis of bacteriophages is facilitated by cryoelectron microscopy and three-dimensional image reconstruction, particle counting, immunoelectron microscopy, and transmission electron microscopy [72].

As can be seen in Fig. 6a, the four viruses being considered are HSV, $Influenza\ A$, $HIV-1$, and $M13\ bacteriophage$ viruses with RI of 1.41, 1.48, 1.5 and 1.57, respectively. When the RI is varied from 1.41 ($HSVvirus$) to 1.57 ($M13\ bacteriophage$), it is obvious that the frequency change for mode f_1 is obvious red shift of the mode (see Fig. 6a). As the absorption peak position is changed due to changes in RI of the material, which is used to detect, one can sense the viruses. In the following, we also calculated and presented the sensitivity of the proposed virus detector device in Fig. 6b. As it is observable from Fig. 6b, the maximum sensitivity is about 76 nm/RIU which is a great value in virus detection devices.

C. Glucose Concentration Sensing in Food Industry for Quality Control Applications

Elevated blood glucose levels can be diagnosed as diabetes. Diabetes can cause and aggravate many diseases, including blindness, kidney failure, heart failure, and so on. Because of the importance of measuring blood glucose concentration, we can use the sensor designed in this article as a diagnostic and control sensor for diabetes. First, we use this sensor to monitor the concentration of water-soluble glucose. As can be seen in Figure 7a, the absorption spectra are plotted for different percentages of water-soluble glucose. The diagram

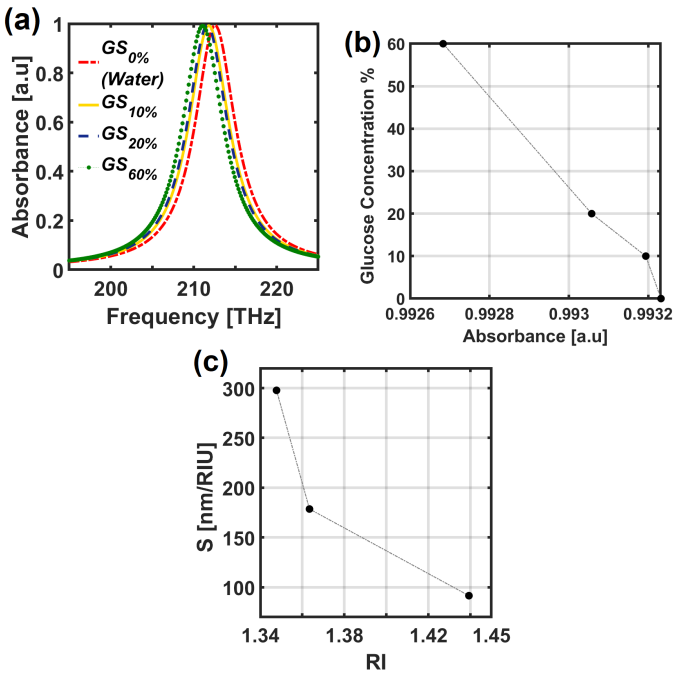

Fig. 7. The reflectance spectra of the different glucose solutions with different RI values vs. frequency. (b) The relation diagram of glucose solution and absorption. And (c) The Sensitivity of the proposed glucose concentration sensor design vs. RI.

TABLE I
THE COMPARISON OF THE SENSOR SENSITIVITY AND DIMENION OF THE STRUCTURE USED IN LITERATURE

Refs.	Sensitivity [nm/RIU]	Dimension of the structure
[73]	19.2	500×1200 nm
[74]	40.6	440×440 nm
[6]	225	600×600 nm
Our work	300	600×600 nm

of absorption changes in the sensor in terms of the percentage of water-soluble glucose is shown in Fig. 7b. As can be seen, the absorption rate of the sensor has a linear relationship with the percentage of water-soluble glucose. This relationship is as follows:

$$\rho = -104541 \times \mathrm{A} + 103836 \tag{1}$$

In this equation, ρ is the percentage of water-soluble glucose and A is the rate of absorption for the used amount of glucose concentration. As can be seen from Fig. 7c, the maximum sensitivity is about $300nm/RIU$ which is a great value in water-soluble glucose concentration sensing.

V. DISCLOSURES

The authors declare no conflicts of interest. There is no funding for this research.

VI. FUTURE OUTLOOK

In this work, plasmonic effects in device structures containing four different metals – Al, Ag, Au, and Cu – are analyzed. Based on this analysis, devices structures are defined which have wide potential for biomedical applications. This plasmonics-based approach facilitates the design of compact detection and measurement devices, and leads to the conception of novel detection modalities, including multi-band

super-absorber nanostructures that are the basis for a variety of nanobiosensors. The rich variety of possible plasmonic-based detectors portents many future applications of plasmonic effects in biomedical applications.

REFERENCES

[1] K. Nakayama, K. Tanabe, and H. A. Atwater, "Plasmonic nanoparticle enhanced light absorption in GaAs solar cells," *Appl. Phys. Lett.*, vol. 93, no. 12, Sep. 2008, Art. no. 121904.

[2] L. Yue, B. Yan, M. Attridge, and Z. Wang, "Light absorption in perovskite solar cell: Fundamentals and plasmonic enhancement of infrared band absorption," *Sol. Energy*, vol. 124, pp. 143–152, Feb. 2016.

[3] S. Song, Q. Chen, L. Jin, and F. Sun, "Great light absorption enhancement in a graphene photodetector integrated with a metamaterial perfect absorber," *Nanoscale*, vol. 5, no. 20, pp. 9615–9619, 2013.

[4] Z. Vafapour, "Large group delay in a microwave metamaterial analog of electromagnetically induced reflectance," *J. Opt. Soc. Amer. A, Opt. Image Sci.*, vol. 35, no. 3, pp. 417–422, 2018.

[5] M. A. Baqir, A. Farmani, T. Fatima, M. R. Raza, S. F. Shaukat, and A. Mir, "Nanoscale, tunable, and highly sensitive biosensor utilizing hyperbolic metamaterials in the near-infrared range," *Appl. Opt.*, vol. 57, no. 33, pp. 9447–9454, 2018.

[6] Z. Vafapour, "Polarization-independent perfect optical metamaterial absorber as a glucose sensor in food industry applications," *IEEE Trans. Nanobiosci.*, vol. 18, no. 4, pp. 622–627, Oct. 2019.

[7] S. Asgari, S. Pooretemad, and N. Granpayeh, "Plasmonic refractive index sensor based on a double concentric square ring resonator and stubs," *Photonics Nanostruct.-Fundamentals Appl.*, vol. 42, Dec. 2020, Art. no. 100857.

[8] H. Zhang *et al.*, "Transparent organic photodetector using a near-infrared absorbing cyanine dye," *Sci. Rep.*, vol. 5, no. 1, p. 9439, Aug. 2015.

[9] L. Liu *et al.*, "Graphene-based polarization-sensitive longwave infrared photodetector," *Nanotechnology*, vol. 30, no. 43, Oct. 2019, Art. no. 435205.

[10] M. Ghodrati, A. Farmani, and A. Mir, "Nanoscale sensor-based tunneling carbon nanotube transistor for toxic gases detection: A first-principle study," *IEEE Sensors J.*, vol. 19, no. 17, pp. 7373–7377, Sep. 2019.

[11] E. S. Lari, Z. Vafapour, and H. Ghahraloud, "Optically tunable triple-band perfect absorber for nonlinear optical liquids sensing," *IEEE Sensors J.*, vol. 20, no. 17, pp. 10130–10137, Sep. 2020.

[12] X. Liu, G. Fu, X. Zhan, and Z. Liu, "All-metal resonant metamaterials for one-, two-, three-band perfect light absorbers and sensors," *Plasmonics*, vol. 14, no. 4, pp. 967–971, Aug. 2019.

[13] Z. Vafapour and H. Ghahraloud, "Semiconductor-based far-infrared biosensor by optical control of light propagation using THz metamaterial," *J. Opt. Soc. Amer. B, Opt. Phys.*, vol. 35, no. 5, pp. 1192–1199, 2018.

[14] D. H. Lien *et al.*, "Nanophotonic devices: Resonance-enhanced absorption in hollow nanoshell spheres with omnidirectional detection and high responsivity and speed (adv. mater. 34/2018)," *Adv. Mater.*, vol. 30, no. 34, 2018, Art. no. 1870257, doi: 10.1002/adma.201870257.

[15] Z. Vafapour, A. Keshavarz, and H. Ghahraloud, "The potential of terahertz sensing for cancer diagnosis," *Heliyon*, vol. 6, no. 12, Dec. 2020, Art. no. e05623.

[16] H. Rabiee-Golgir *et al.*, "Ultra-thin super absorbing photon trapping materials for high-performance infrared detection," in *Proc. 45th Infr. Technol. Appl., Int. Soc. Opt. Photon.*, vol. 11002, 2019, Art. no. 110020T, doi: 10.1117/12.2518690.

[17] J. Chen *et al.*, "Optical nano-imaging of gate-tunable graphene plasmons," *Nature*, vol. 487, no. 7405, p. 77, 2012.

[18] B. Deng *et al.*, "Coupling-enhanced broadband mid-infrared light absorption in graphene plasmonic nanostructures," *ACS Nano*, vol. 10, no. 12, pp. 11172–11178, Dec. 2016.

[19] N. A. Aghamiri, F. Huth, A. J. Huber, A. Fali, R. Hillenbrand, and Y. Abate, "Hyperspectral time-domain terahertz nano-imaging," *Opt. Exp.*, vol. 27, no. 17, pp. 24231–24242, 2019.

[20] F. Bagci and B. Akaoglu, "Influences of supercell termination and lateral row number on the determination of slow light properties of photonic crystal waveguides," *Optik-Int. J. Light Electron Opt.*, vol. 124, no. 21, pp. 4739–4743, Nov. 2013.

[21] Z. Vafapour, "Slowing down light using terahertz semiconductor metamaterial for dual-band thermally tunable modulator applications," *Appl. Opt.*, vol. 57, no. 4, pp. 722–729, 2018.

[22] F. Bagci and B. Akaoglu, "Enhancement of buffer capability in slow light photonic crystal waveguides with extended lattice constants," *Opt. Quantum Electron.*, vol. 47, no. 3, pp. 791–806, Mar. 2015.

[23] Z. Vafapour, "Slow light modulator using semiconductor metamaterial," in *Proc. 22nd Integr. Opt., Devices, Mater. Technol., Int. Soc. Opt. Photon.*, vol. 10535, 2018, Art. no. 105352A, doi: 10.1117/12.2292259.

[24] B. Zhang *et al.*, "Absorption and slow-light analysis based on tunable plasmon-induced transparency in patterned graphene metamaterial," *Opt. Exp.*, vol. 27, no. 3, pp. 3598–3608, 2019.

[25] T. Inoue, T. Asano, M. De Zoysa, A. Oskooi, and S. Noda, "Design of single-mode narrow-bandwidth thermal emitters for enhanced infrared light sources," *J. Opt. Soc. Amer. B, Opt. Phys.*, vol. 30, no. 1, pp. 165–172, 2013.

[26] S. Ghafari, M. R. Forouzeshfard, and Z. Vafapour, "Thermo optical switching and sensing applications of an infrared metamaterial," *IEEE Sensors J.*, vol. 20, no. 6, pp. 3235–3241, Mar. 2020.

[27] Z. Vafapour and A. Zakery, "New regime of plasmonically induced transparency," *Plasmonics*, vol. 10, no. 6, pp. 1809–1815, Dec. 2015.

[28] H. E. Nejad, A. Mir, and A. Farmani, "Supersensitive and tunable nano-biosensor for cancer detection," *IEEE Sensors J.*, vol. 19, no. 13, pp. 4874–4881, Jul. 2019.

[29] F. Bagci, A. Fernández-Prieto, A. Lujambio, J. Martel, J. Bernal, and F. Medina, "Compact balanced dual-band bandpass filter based on modified coupled-embedded resonators," *IEEE Microw. Wireless Compon. Lett.*, vol. 27, no. 1, pp. 31–33, Jan. 2017.

[30] P. K. Singh, K. A. Korolev, M. N. Afsar, and S. Sonkusale, "Single and dual band 77/95/110 GHz metamaterial absorbers on flexible polyimide substrate," *Appl. Phys. Lett.*, vol. 99, no. 26, Dec. 2011, Art. no. 264101.

[31] H. R. Seren *et al.*, "Optically modulated multiband terahertz perfect absorber," *Adv. Opt. Mater.*, vol. 2, no. 12, pp. 1221–1226, Dec. 2014.

[32] Z. Vafapour and M. R. Forouzeshfard, "Disappearance of plasmonically induced reflectance by breaking symmetry in metamaterials," *Plasmonics*, vol. 12, no. 5, pp. 1331–1342, Oct. 2017.

[33] S. Asgari, N. Granpayeh, and T. Fabritius, "Controllable terahertz cross-shaped three-dimensional graphene intrinsically chiral metastructure and its biosensing application," *Opt. Commun.*, vol. 474, Nov. 2020, Art. no. 126080.

[34] J. Wang *et al.*, "Tunable broad-band perfect absorber by exciting of multiple plasmon resonances at optical frequency," *Opt. Exp.*, vol. 20, no. 14, pp. 14871–14878, 2012.

[35] Y. Qu *et al.*, "Spatially and spectrally resolved narrowband optical absorber based on 2D grating nanostructures on metallic films," *Adv. Opt. Mater.*, vol. 4, no. 3, pp. 480–486, Mar. 2016.

[36] E. E. Narimanov and A. V. Kildishev, "Optical black hole: Broadband omnidirectional light absorber," *Appl. Phys. Lett.*, vol. 95, no. 4, Jul. 2009, Art. no. 041106.

[37] M. R. Forouzeshfard, S. Ghafari, and Z. Vafapour, "Solute concentration sensing in two aqueous solution using an optical metamaterial sensor," *J. Lumin.*, vol. 230, Feb. 2021, Art. no. 117734.

[38] J. Yang *et al.*, "Broadband terahertz absorber based on multi-band continuous plasmon resonances in geometrically gradient dielectric-loaded graphene plasmon structure," *Sci. Rep.*, vol. 8, no. 1, p. 3239, Dec. 2018.

[39] L. Ye, F. Zeng, Y. Zhang, and Q. H. Liu, "Composite graphene-metal microstructures for enhanced multiband absorption covering the entire terahertz range," *Carbon*, vol. 148, pp. 317–325, Jul. 2019.

[40] Z. Yin *et al.*, "Optically transparent and single-band metamaterial absorber based on indium-tin-oxide," *Int. J. RF Microw. Comput.-Aided Eng.*, vol. 29, no. 2, Feb. 2019, Art. no. e21536.

[41] Y. Ma, Q. Chen, J. Grant, S. C. Saha, A. Khalid, and D. R. S. Cumming, "A terahertz polarization insensitive dual band metamaterial absorber," *Opt. Lett.*, vol. 36, no. 6, pp. 945–947, 2011.

[42] H. Xu, L. Hu, Y. Lu, J. Xu, and Y. Chen, "Dual-band metamaterial absorbers in the visible and near-infrared regions," *J. Phys. Chem. C*, vol. 123, no. 15, pp. 10028–10033, Apr. 2019.

[43] H.-T. Chen, "Interference theory of metamaterial perfect absorbers," *Opt. Exp.*, vol. 20, no. 7, pp. 7165–7172, 2012.

[44] W. Li and J. Valentine, "Metamaterial perfect absorber based hot electron photodetection," *Nano Lett.*, vol. 14, no. 6, pp. 3510–3514, Jun. 2014.

[45] A. Ghobadi, H. Hajian, B. Butun, and E. Ozbay, "Strong light-matter interaction in lithography-free planar metamaterial perfect absorbers," *ACS Photon.*, vol. 5, no. 11, pp. 4203–4221, 2018.

[46] W. Wang, X. Yang, T. S. Luk, and J. Gao, "Enhanced quantum dots spontaneous emission with metamaterial perfect absorbers," *Appl. Phys. Lett.*, vol. 114, no. 2, Jan. 2019, Art. no. 021103.

[47] A. Farmani, "Three-dimensional FDTD analysis of a nanostructured plasmonic sensor in the near-infrared range," *J. Opt. Soc. Amer. B, Opt. Phys.*, vol. 36, no. 2, pp. 401–407, 2019.
[48] N. Liu *et al.*, "Plasmonic analogue of electromagnetically induced transparency at the Drude damping limit," *Nature Mater.*, vol. 8, no. 9, pp. 758–762, Sep. 2009.
[49] P. H. Lissberger and R. G. Nelson, "Optical properties of thin film au-MgF_2 cermets," *Thin Solid Films*, vol. 21, no. 1, pp. 159–172, Mar. 1974.
[50] A. Cusano *et al.*, "Coated long-period fiber gratings as high-sensitivity optochemical sensors," *J. Lightw. Technol.*, vol. 24, no. 4, pp. 1776–1786, Apr. 2006.
[51] Z. Vafapour, "Near infrared biosensor based on classical electromagnetically induced reflectance (Cl-EIR) in a planar complementary metamaterial," *Opt. Commun.*, vol. 387, pp. 1–11, Mar. 2017.
[52] J. A. Stewart, T. C. Holland, and A. S. Bhagwat, "Human herpes simplex virus-1 depletes APOBEC3A from nuclei," *Virology*, vol. 537, pp. 104–109, Nov. 2019.
[53] C. M. Menendez and D. J. J. Carr, "Defining nervous system susceptibility during acute and latent herpes simplex virus-1 infection," *J. Neuroimmunol.*, vol. 308, pp. 43–49, Jul. 2017.
[54] C. M. Kollias, R. B. Huneke, B. Wigdahl, and S. R. Jennings, "Animal models of herpes simplex virus immunity and pathogenesis," *J. NeuroVirol.*, vol. 21, no. 1, pp. 8–23, Feb. 2015.
[55] D. M. Knipe and A. Cliffe, "Chromatin control of herpes simplex virus lytic and latent infection," *Nature Rev. Microbiol.*, vol. 6, no. 3, p. 211, 2008.
[56] A. V. Farooq and D. Shukla, "Herpes simplex epithelial and stromal keratitis: An epidemiologic update," *Surv. Ophthalmol.*, vol. 57, no. 5, pp. 448–462, Sep. 2012.
[57] J. LeGoff, H. Péré, and L. Bélec, "Diagnosis of genital herpes simplex virus infection in the clinical laboratory," *Virol. J.*, vol. 11, no. 1, p. 83, Dec. 2014.
[58] S. Zhang *et al.*, "P-STAT1 regulates the influenza a virus replication and inflammatory response *in vitro* and vivo," *Virology*, vol. 537, pp. 110–120, Nov. 2019.
[59] M. Jané *et al.*, "Epidemiological and clinical characteristics of children hospitalized due to influenza A and B in the south of Europe, 2010–2016," *Sci. Rep.*, vol. 9, no. 1, pp. 1–7, Dec. 2019.
[60] T. Shi *et al.*, "Mortality risk factors in children with severe influenza virus infection admitted to the pediatric intensive care unit," *Medicine*, vol. 98, no. 35, 2019, Art. no. e16861.
[61] K. W. Hong, H. J. Cheong, J. Y. Song, J. Y. Noh, T. U. Yang, and W. J. Kim, "Clinical manifestations of influenza A and B in children and adults at a tertiary hospital in Korea during the 2011–2012 season," *Jpn. J. Infectious Diseases*, vol. 68, no. 1, pp. 20–26, 2015.
[62] C. Paules and K. Subbarao, "Influenza," *Lancet*, vol. 390, no. 10095, pp. 697–708, 2017.
[63] A. Woźniak-Kosek, B. Kempińska-Mirosławska, and G. Hoser, "Detection of the influenza virus yesterday and now," *Acta Biochimica Polonica*, vol. 61, no. 3, pp. 465–470, Sep. 2014.
[64] E. Fanales-Belasio, M. Raimondo, B. Suligoi, and S. Buttò, "HIV virology and pathogenetic mechanisms of infection: A brief overview," *Annali dell Istituto Superiore di Sanita*, vol. 46, no. 1, pp. 5–14, Mar. 2010.
[65] B. N. R. Dube, T. P. Marshall, and R. P. Ryan, "Predictors of human immunodeficiency virus (HIV) infection in primary care: A systematic review protocol," *Systematic Rev.*, vol. 5, no. 1, p. 158, Dec. 2016.
[66] *Global HIV AIDS Statistics—2018 Fact Sheet*, UNAIDS, Geneva, Switzerland, 2019.
[67] K. C. Abbott, I. Hypolite, P. G. Welch, and L. Y. Agodoa, "Human immunodeficiency virus/acquired immunodeficiency syndrome-associated nephropathy at end-stage renal disease in the United States: Patient characteristics and survival in the pre highly active antiretroviral therapy era," *J. Nephrol.*, vol. 14, no. 5, pp. 377–383, 2001.
[68] C. A. Agutu *et al.*, "Systematic review of the performance and clinical utility of point of care HIV-1 RNA testing for diagnosis and care," *PLoS ONE*, vol. 14, no. 6, Jun. 2019, Art. no. e0218369.
[69] C. Weigel and H. Seitz, "Bacteriophage replication modules," *FEMS Microbiol. Rev.*, vol. 30, no. 3, pp. 321–381, May 2006.
[70] S. L. Díaz-Muñoz and B. Koskella, "Bacteria–phage interactions in natural environments," in *Advances in Applied Microbiology*, vol. 89. New York, NY, USA: Academic, 2014, pp. 135–183.
[71] L. A. Ogilvie and B. V. Jones, "The human gut virome: A multifaceted majority," *Frontiers Microbiol.*, vol. 6, p. 918, Sep. 2015.
[72] H. W. Ackermann, "Bacteriophage electron microscopy," in *Advances in Virus Research*, vol. 82. New York, NY, USA: Academic, 2012, pp. 1–32.
[73] X.-J. He, L. Wang, J.-M. Wang, X.-H. Tian, J.-X. Jiang, and Z.-X. Geng, "Electromagnetically induced transparency in planar complementary metamaterial for refractive index sensing applications," *J. Phys. D, Appl. Phys.*, vol. 46, no. 36, Sep. 2013, Art. no. 365302.
[74] M. Wan, S. Yuan, K. Dai, Y. Song, and F. Zhou, "Electromagnetically induced transparency in a planar complementary metamaterial and its sensing performance," *Optik*, vol. 126, no. 5, pp. 541–544, Mar. 2015.